PRELIMINARY EXPERIMENTS OF A FLAPPING WING IN THREE-DEGREE-OF-FREEDOM MOTIONS

X. Huang and T. Brown
Aerodynamics Laboratory
Institute for Aerospace Research
National Research Council of Canada

Keywords: *flapping wing aerodynamics, water tunnel experiment, three-degree-of-freedom*

Abstract

A preliminary water tunnel experiment was conducted on an insect wing performing three degree-of-freedom (3DOF) motions. A bi-fold five-component strain-gauge balance has been developed to measure the aerodynamic behavior of insect's flapping wings.

It has been found that at low- to mid-range angles of attack, the normal force and pitching moment of the wing increase as the angle of attack increases. While at high angles of attack, the phase shift between the motion and the aerodynamic loads becomes obvious. The maximum normal force appears some distance ahead of the maximum angle of attack and decreases dramatically thereafter as the angle increases further.

Introducing second and third degrees of freedom motions could further increase the maximum normal force compared with one-degree-of freedom motion, indicating possible delayed stall caused by the additional motion.

1. Introduction

There is keen interest in insects' flapping wing aerodynamics. To support the insects' body weight, their wings typically produce two to three times more lift than can be accounted for by conventional aerodynamics [1]. Research results from biologists and zoologists show that insects with flapping wings can fly thousands of miles at extremely high lift-to-drag ratios and with great stability and maneuverability which cannot be explained by conventional aerodynamic principles. It is hoped that a better understanding of aerodynamics and flight dynamics of these highly successful creatures might provide better insights towards the design of realistic micro air vehicles.

Although the solution is not clear at this time, insects' flapping wings have at least three remarkable features: 1) complex three degree-of-freedom motions, 2) deforming wing structure during the motion history, and 3) micro surface devices for active flow control (Fig. 1 and Fig. 2). With these features insects achieve their excellent aerodynamic performance by delayed stall, rotational circulation, wake capture and further interplay of these mechanisms. For a hovering Hawkmoth [2], for example, the vortical unsteady and highly non-linear flow at low Reynolds numbers, caused by rapid up/down stroke in combination with rotating motions about its long axis and tilting of the wings to appropriate angles, must be responsible for creating sufficient lift and control power (Fig. 1). Understanding the complex aerodynamic flow around the insect as it is controlled by these remarkable features is a prerequisite to building a real robotic "insect".

In the past few years, much progress has been made in revealing the unsteady high-lift mechanisms of flapping wings [3]. Among others, Dickinson et al. have developed instruments and procedures used in their experiments to measure the two-dimensional forces (lift and drag) in still fluid [4, 5]. However, as the high aerodynamic performance of insect's wings is achieved by 3DOF motions, it will be very important to study its aerodynamic behavior under 3DOF conditions. Thus, a 3DOF system, i.e. pitch motion (α), dihedral motion (γ) and sweep motion (Λ), has been developed and the preliminary experimental studies were

conducted on a flapping wing in the IAR water tunnel. This paper presents the development of the experimental techniques and some preliminary experimental results.

2. Experimental set-up

The experiments were conducted in the IAR water tunnel (Fig. 3). The water tunnel has an open surface test section with a vertical return circuit. The test section is 15in wide and 20in high. The free-stream turbulence level in the tunnel is rated at $u'/U_\infty<1\%$. Much care was exercised in ensuring that the turbulence screens were always free of trapped air bubbles and that a constant temperature of 22°C~ 24°C was maintained. The uniformity of the velocity field in the empty tunnel has been validated by the PIV measurements at all Reynolds number conditions of interest.

A half model test method was used in the experiments (Fig. 4). An insect-like wing was set vertically in the water flow. Except for the wing, all of the equipment was above the water surface, including a 3DOF gearbox, a 3DOF control system and a small five-component strain gauge balance (Fig. 5 to Fig. 7).

The 3DOF system controlled three angular motions: pitch motion (α), dihedral motion (γ) and sweep motion (Λ). The standard terminologies and nomenclatures used in fixed wing aerodynamics are adopted here. The body axes system is shown in Fig. 8. Three angles are taken as the motion parameters, i.e. angle of attack (α), sweep angle (Λ) and dihedral angle (γ), corresponding to feathering motion angle, elevation angle and position angle in some bioflight literature. For example, Fig. 9a shows the three angular motion histories. The consonant wing tip motion history is shown in Fig. 9b.

Pitch angle was mechanically independent but sweep angle and dihedral angle were mechanically linked such that actuating either motor caused the other angle to move. The interaction relationship between sweep angle and dihedral angle is 1:1, degree for degree. That is, if the sweep angle is commanded to move one degree, the dihedral angle will also move one degree and vice versa. Therefore the equations of motion for these two axes will reflect the interdependent relationship by subtracting one angle from the other.

The gear ratio between the motors and the wing angles was the same for all three axes and equalled 1245:1, 415:1 through the gearhead and 3:1 through the open gearing. One motor revolution caused 0.29° deflection in wing angle. Although the maximum no-load speed of the motors is 28,000 rpm, the maximum continuous motor speed recommended for the gearhead was 5,000 rpm, making the maximum recommended rate of change in wing angles equal to 24°/s. The stall torque for the motor was 1.6 oz-in. But the recommended continuous motor torque load for 5,000 rpm is 0.42 oz-in. and the recommended maximum continuous torque output from the gearhead is 42.5 oz-in. generated by 0.18 oz-in of motor torque, well within the motor's capability. This translates to a maximum torque available at the wing center of rotation of approximately 100 oz-in for pitching moment and yawing moment and 65 oz-in for rolling moment. Rolling moment is reduced by two additional sets of 80% efficient gears and bearings that the other axes do not have. The instantaneous torque values are permitted 150% higher than the continuous values. The system was carefully adjusted to reduce the backlash. However it has been found that there was about 1° in yawing motion which causes some inaccuracy in the measurements and has to be improved in the near future.

The 3DOF system was controlled by three stepping motors. Faulhaber 1628T012BK312 brushless motors, Series 16/7 415:1 gearhead and HEM1626T16 encoder were installed and connected to the gearbox. The LabView software was used to control the motors that actuated the 3-axes-of-motion gearbox. Model motion programming also included safety limits: 1) load limits provided by the strain gauge balance output, 2) torque (current) limits on the motors, 3) a warning to the operator if limits were approached and 4) halt the motion if limits were exceeded.

A Discrete Fourier Transform (DFT) program computed on equal frequency intervals. The related motion control system was determined by Fourier series in the corresponding Fourier equations:

$$F(t) = a_0 + \Sigma a_n \cos(n * kt) + b_n \sin(n * kt)$$

The results in the Fourier equations composed of four parts: real part, imaginary part, correspond frequency and amplitude. The Inversed Fourier Transform (IFT) was used to transfer the output into the time domain. A trail candidate in the Fourier equations was adopted by analyzing the flapping motions in [5]. In that example the following Fourier series were taken as shown in the table below:

	Pitching motion		Yawing motion		Rolling motion	
n	an	bn	an	bn	an	bn
0	-0.8615	0.0000	-0.1653	0.0000	1.9644	0.0000
1	-0.1255	1.1978	1.6732	0.2239	1.7860	0.7745
2	0.0233	0.1214	0.4018	-0.1053	0.3367	-0.0280
3	-0.1048	0.1477	0.1002	0.0154	0.1936	0.0960
4	-0.0097	0.1958	-0.0115	0.0314	0.0691	0.0408
5	0.0894	0.1017	0.0110	0.0355	0.0134	0.0004
6	0.0503	0.0403				
7	0.0399	0.0634				
8	0.0377	0.0410				
9	0.0227	0.0170				

A healthy comparisons between calculated and raw data as shown in Fig. 10a through Fig. 10c are resource of confidence in the program.

The five-component strain gauge balance supported the wing on one end and was connected to the motion system on other end (Fig. 5b). The balance consists of five elements corresponding to each aerodynamic force or moment including normal force (N), drag (X), pitching moment (m_z), yawing moment (m_y) and rolling moment (m_x). Figure 8 shows the coordinate axes system. As seen from Fig. 3b, the rotation center of the wing was above the balance reference center. In order to mimic real insect's flight, it is important to shorten the length of the balance as much as possible. However, shortening the length of the elements in the balance reduces sensitivity. Thus a new concept of bi-fold concept was introduced as shown in Fig. 11 which shows all parts before their assembly. Not like conventional balances where the length of the balance is the sum of each element, the new concept of the bi-fold balance makes the length of each element close to the length of the total balance. It also has the advantages of easy manufacturing, gauging and wiring. The calibration results confirm that the balance satisfies the experimental requirements.

An insect-like wing model was used in the experiments. Its section view, plan view and 3D view are shown in Fig. 12. The corresponding plan and section coordinates are listed in Table 1. The model was constructed using a rapid prototyping (RP) and Stereolithography technique at IAR. The laser beam was guided by an X-Y stage that followed the computerized coordinates of the 3D object. The surface details resolved to 3μm. The resulting model is a rigid solidified photopolymer. It is a solid wing model and obviously lacks the deformability of a real, feathered wing.

3. Preliminary Experimental Results and Discussions

The aerodynamic loads and motions were recorded synchronously during the experiments with a maximum sample rate of 100/sec. Different motion profiles were tested – from 1DOF (pitching motion) to 3DOF motion. The ranges of angle of attack, sweep angle and dihedral angle were ±60º, ±20º and ±20º respectively. The test Reynolds number, based on the mean aerodynamic chord (1.5in), ranged from $5x10^3$ to $10x10^3$. The reference area for coefficients is the wing plan area. The reference length for pitching moment is the mean aerodynamic chord while for yawing and rolling moment, it is the wing span (5in). The reference centers for the three moment coefficients are in the center of the balance, which can be found in Fig. 5b.

Samples of preliminary results are shown from Fig. 13 to Fig. 15. As more experiments will be conducted in the near future, here only brief analysis and discussions are given for these preliminary experimental results.

Figure.13 presents the results for 1DOF (pitching motion) from α=-2º to 20º, where Fig. 13a is the motion profile and Fig. 13b shows the measured coefficients. The coefficients of pitching moment (m_z) and normal force (C_N) increase as the angle of attack increases until the angle of attack reaches a maximum of 20º and then decreases as α decreases. The almost synchronous increase of pitching moment and normal force indicates that the location of center of pressure may not change too much as the angle changes.

Figure 14 shows results for the angle of attack in the range of α=-8º to 60º. Compared with Fig. 13 it can be seen that the maximum normal force does not increase linearly as the angle of attack increases. Moreover, the maximum normal force appears at $\alpha\approx$40º. Further increase of angle of attack results in the dramatic decrease in normal force and pitching moment. It indicates that the stall happens when α>40º and eventually occurs over the whole wing area. Nevertheless, the maximum normal force coefficient could reach C_N=1.2 at $\alpha\approx$40º.

Compared with 1DOF motion, the 3DOF motion brings more interesting results as seen in Fig. 15. The wing performs 3DOF motion as shown in Fig. 15a and the corresponding aerodynamic coefficients are shown in Fig. 15b. The pitching motion in 3DOF motions (Fig. 15a) is the same as 1DOF motion in Fig. 14a but two other motions are added: sweep motion and dihedral motion. Compared with Fig. 14b it can be observed that the maximum normal force could reach C_N=1.4. It may indicate that there is some delayed stall as 3DOF motion is involved. Also the drag in Fig. 15b is higher than that in Fig. 14b. Comparing 1DOF with 3DOF motion results, one finds that the aerodynamic coefficients exhibit quite different behavior. Dihedral and sweep motion could increase the maximum normal force and expand its area. Also it will create higher negative force when the wing is in upstroke. This negative force is actually a thrust when the angle of attack is larger than 90º, as the wing uses the mechanism of wake capture.

It should be mentioned that the measured aerodynamic loads are not very smooth, even for one-degree-of-freedom motions at low angles of attack (Fig. 13b). The data reported in those figures were recorded at Δt=0.03. No smoothing techniques were used in the data reduction. Also, mechanical backlash was checked before each test. It was found that only the sweep motion had 1º of backlash. Thus it is not very clear at this time what causes the unsmooth behavior. Nevertheless, we can still, in general, observe some important characteristics from these experimental results.

In order to further investigate the flow behavior, the uncertainty caused by backlash in the mechanism should be minimized or eliminated. Also, flow visualization studies should be conducted in future experiments in order to fully understand the flow behavior.

4. Conclusions

- A three-degree-of-freedom motion system including a bi-fold five-component strain-gauge balance has been developed which can be applied to study the aerodynamic behavior of insect's flapping wings.
- At low to mid-range angles of attack, the normal force and pitching moment of the tested insect-like wing increase as the angle of attack increases.
- At high angles of attack, a distinct phase shift between the applied motion and aerodynamic loads recovered on the wing is noted. The maximum normal force appears ahead of the maximum angle of attack. After that angle, the normal force reduces dramatically as the angle increases further, indicating that stall develops over the wing.
- Three-degree-of-freedom motion could further increase the maximum normal force compared with one-degree-of-freedom motion, indicating possible delayed stall by the 3DOF motion.

Acknowledgement

The work was partly supported by the Department of the National Defence Canada / DRDC under the Collaboration Agreement: "Flapping Wings Aerodynamics for Efficient Insect-Size Aircrafts."

5. References

[1] Ellington, C.P., "The Novel Aerodynamics of Insect Flight: Application to Micro-Air Vehicles," The *Journal of Experimental Biology* 202, 3439-3448, 1999.

[2] Liu, H. and Kawachi, K., "Leading-Edge Vortices of Flapping and Rotary Wings at Low Reynolds Number," *Progress in Astronautics and Aeronautics*, 2001, Chapter 14, Vol. 195.

[3] Mueller, T.J., "Fixed and Flapping Wing Aerodynamics for Micro Air Vehicle Application," *Progress in Astronautics and Aeronautics*, Vol. 195, 2001.

[4] Dickinson, M.H., Lehmann, F.O. and Sane, S.P., "Wing Rotation and the Aerodynamic Basis of Insect Flight". *Science* 284, 1954-1960, 1999.

[5] Sane, S.P., and Dickinson, M.H., "The Control of Flight Force by a Flapping Wing: Lift and Drag Production," *Journal of Experimental Biology* 204, 2607-2626, 2001.

[6] Huang, X.Z., Wong, F., Brown, T., and Berlivet T., "Development of Bi-Fold Water-Tunnel Half Model Balance," LR-AL-2005-0066.

Table 1 wing coordinates (plan view)

x	y (TE)	x	y (LE)	c
0.0000	0.1700	0.0000	0.4991	0.3291
0.0652	0.1680	0.0652	0.4991	0.3311
0.1369	0.1600	0.1369	0.4997	0.3397
0.2087	0.1550	0.2087	0.5003	0.3453
0.2739	0.1350	0.2739	0.5006	0.3706
0.3325	0.1100	0.3325	0.4997	0.3897
0.3977	0.0660	0.3977	0.5027	0.4427
0.4695	0.0020	0.4695	0.5091	0.5071
0.5347	-0.0650	0.5347	0.5169	0.5869
0.5999	-0.1800	0.5999	0.5287	0.7067
0.6716	-0.4400	0.6716	0.5394	0.9794
0.7303	-0.6400	0.7303	0.5507	1.1907
0.8020	-0.7700	0.8020	0.5619	1.3319
0.8672	-0.8600	0.8672	0.5714	1.4314
0.9389	-0.9500	0.9389	0.5779	1.5279
0.9976	-1.0000	0.9976	0.5827	1.5827
1.0628	-1.0500	1.0628	0.5910	1.6410
1.1476	-1.1090	1.1476	0.5993	1.6993
1.2976	-1.1900	1.2976	0.6094	1.7994
1.4606	-1.2448	1.4606	0.6165	1.8613
1.6171	-1.2804	1.6171	0.6242	1.9046
1.7866	-1.3041	1.7866	0.6325	1.9366
1.9431	-1.3219	1.9431	0.6366	1.9585
2.1191	-1.3272	2.1191	0.6402	1.9674
2.2756	-1.3278	2.2756	0.6402	1.9680
2.4321	-1.3219	2.4321	0.6461	1.9680
2.6147	-1.3041	2.6147	0.6461	1.9502
2.7777	-1.2833	2.7777	0.6461	1.9295
2.9277	-1.2626	2.9277	0.6461	1.9087
3.0907	-1.2318	3.0907	0.6437	1.8755
3.2537	-1.1962	3.2537	0.6427	1.8389
3.4167	-1.1559	3.4167	0.6414	1.7973
3.5862	-1.1097	3.5862	0.6402	1.7499
3.7558	-1.0634	3.7558	0.6372	1.7007
3.9253	-1.0077	3.9253	0.6319	1.6396
4.0883	-0.9484	4.0883	0.6283	1.5768
4.2513	-0.8951	4.2513	0.6218	1.5169
4.4209	-0.8299	4.4209	0.6106	1.4404
4.5774	-0.7676	4.5774	0.5910	1.3586
4.7534	-0.6906	4.7534	0.5661	1.2567
4.9210	-0.6150	4.9210	0.5335	1.1485
5.0788	-0.5365	5.0788	0.4713	1.0077
5.1401	-0.4967	5.1401	0.4400	0.9235
5.2111	-0.4535	5.2111	0.4050	0.8435
5.2822	-0.3983	5.2822	0.3490	0.7362
5.3533	-0.3379	5.3533	0.2900	0.6046
5.4257	-0.2650	5.4257	0.2015	0.4665
5.4772	-0.1800	5.4772	0.0966	0.2922
5.5000	0.0000	5.5000	0.0000	0.0000

wing section coordinates

x	z (upper)	x	z (lower)
0.0002	0.0000	0.0002	0.0000
0.0010	0.0310	0.0010	-0.0280
0.0030	0.0540	0.0030	-0.0530
0.0070	0.0800	0.0070	-0.0800
0.0110	0.0960	0.0110	-0.0946
0.0153	0.1049	0.0153	-0.1059
0.0446	0.1648	0.0348	-0.1304
0.1423	0.3387	0.0934	-0.1958
0.2497	0.4897	0.1911	-0.2813
0.3571	0.6068	0.2985	-0.3485
0.4450	0.6822	0.4255	-0.4010
0.5231	0.7366	0.5915	-0.4403
0.6403	0.8004	0.7380	-0.4578
0.7380	0.8405	0.9626	-0.4681
0.8258	0.8689	1.2070	-0.4692
0.9333	0.8959	1.5290	-0.4631
1.0600	0.9198	2.0470	-0.4306
1.5190	0.9706	2.5250	-0.3610
2.0370	1.0084	3.0330	-0.2423
2.5250	1.0361	3.5310	-0.0967
3.0330	1.0492	4.0390	0.0584
3.5410	1.0428	4.5370	0.1975
4.0490	1.0212	5.0540	0.3159
4.5660	0.9899	5.5430	0.3980
5.0640	0.9537	6.0410	0.4488
5.5430	0.9109	6.5390	0.4641
6.0600	0.8503	7.0370	0.4426
6.5490	0.7753	7.5350	0.3862
7.0470	0.6815	8.0520	0.2982
7.5450	0.5758	8.5600	0.1940
8.0520	0.4631	9.0580	0.0822
8.5600	0.3462	9.5470	-0.0394
9.0680	0.2147	10.0450	-0.1802
9.5470	0.0616	10.3850	-0.2693
10.0450	-0.1205		
10.3850	-0.2126		

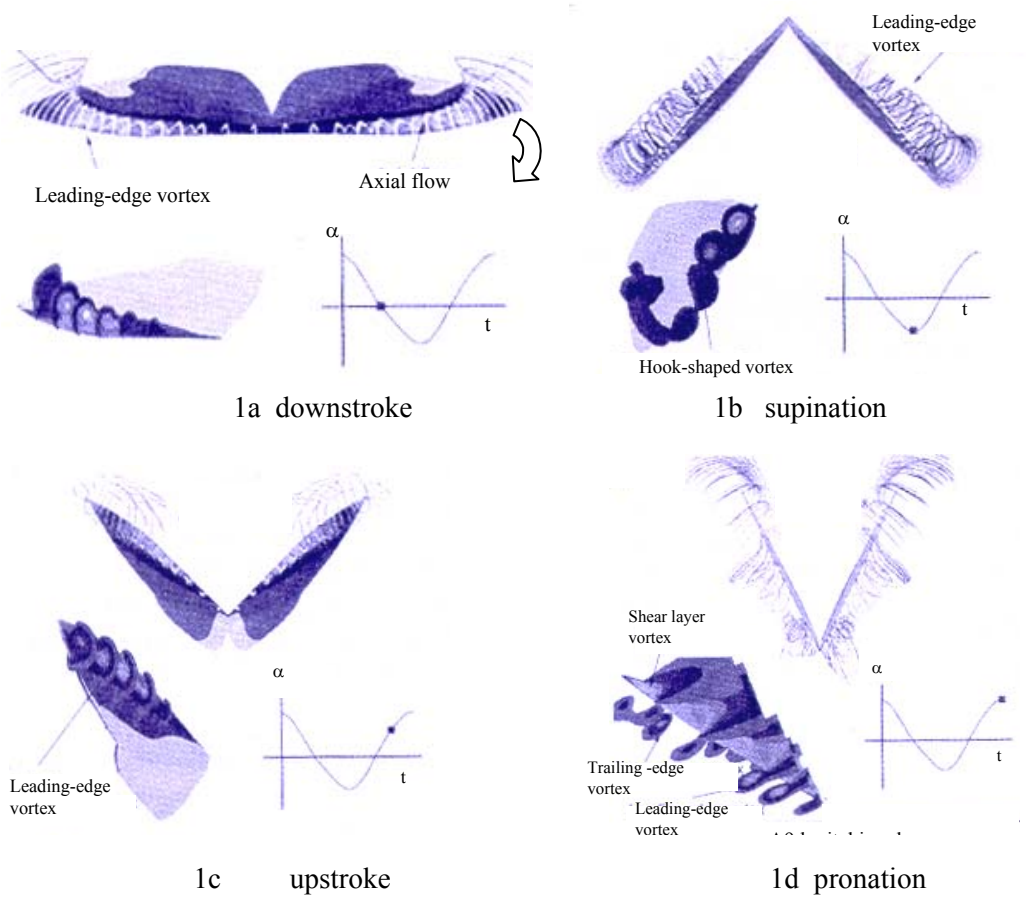

1a downstroke 1b supination

1c upstroke 1d pronation

Fig. 1 Dynamic vortex structure around a flapping wing during a complete wing beat cycle[2]

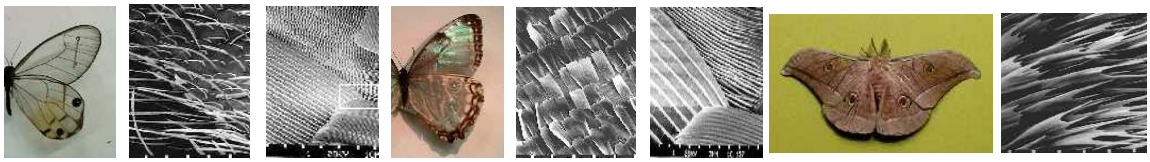

Fig. 2 Complex feather patterns on insect's wing surfaces

Fig. 3 IAR 1520 water tunnel

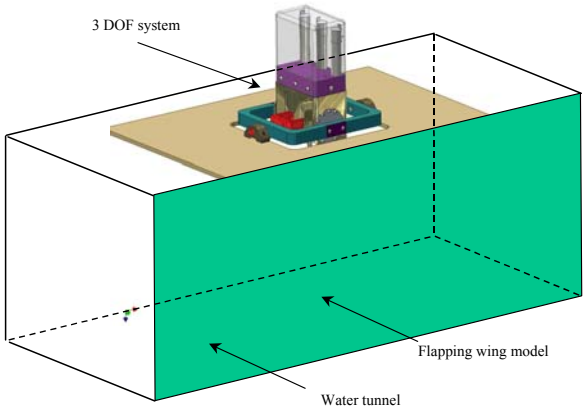

Fig. 4 Schematic 3DOF system set-up

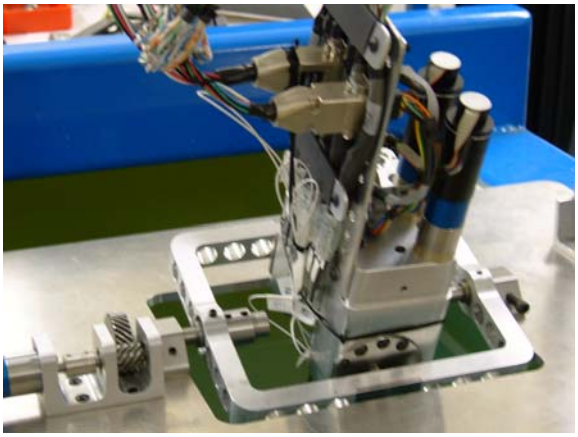

5a top view

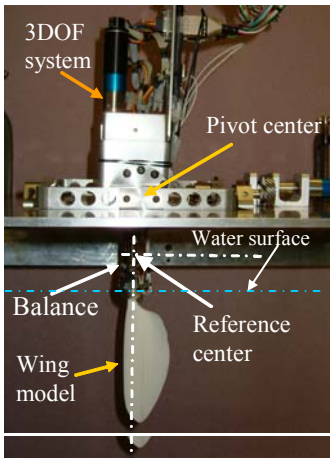

5b side view

Fig. 5 Three-degree-of-freedom motion system installed in the IAR water tunnel

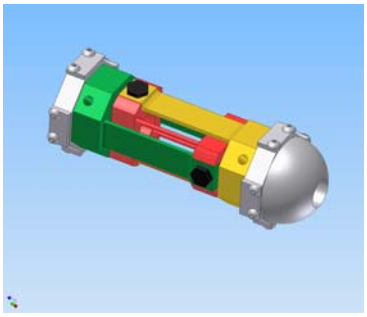

Fig. 6 Five-component strain gauge balance

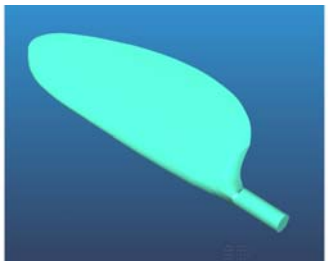

Fig. 7 Insect-like wing model

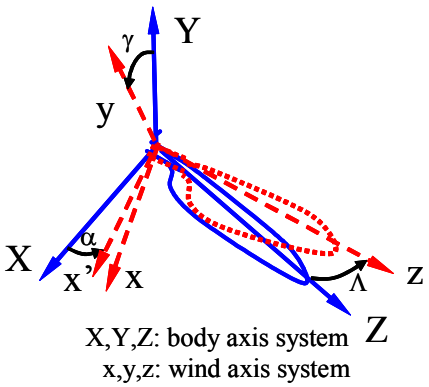

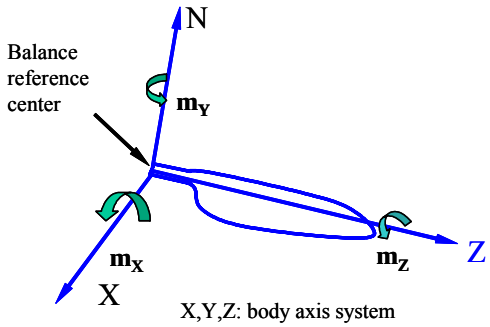

Fig. 8 Coordinate system

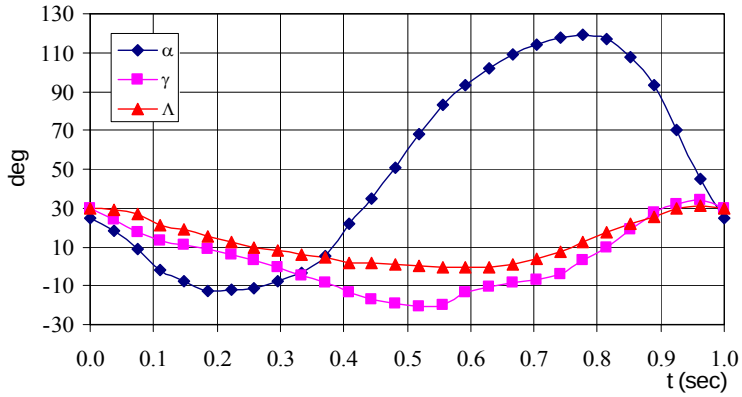

9a Sample of three motion parameters' histories

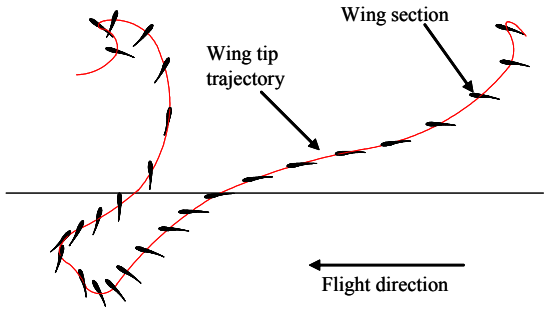

9b consonant wing tip motion history

Fig. 9 Motion profile and corresponding parameters

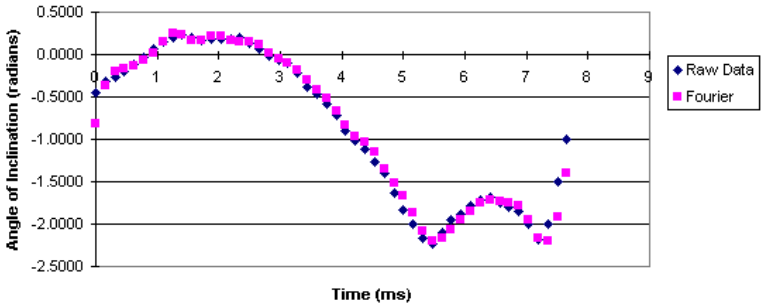

10a Comparisons in Pitching motion

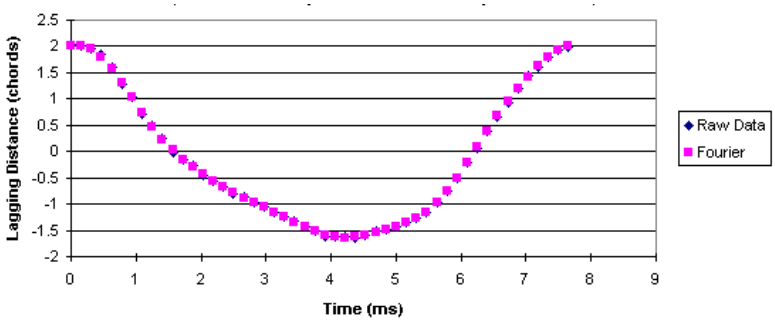

10b Comparisons in yawing motion

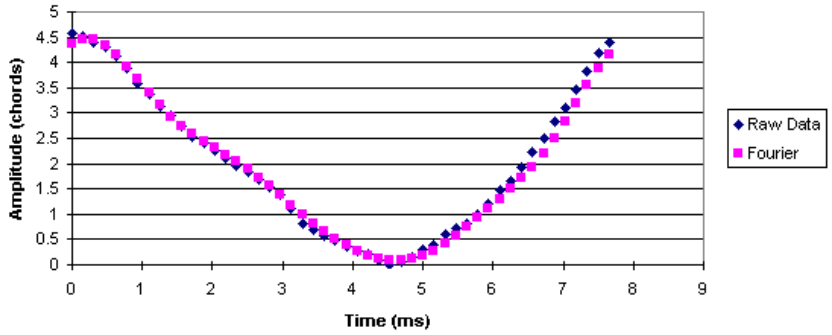

10c Comparisons in dihedral motion

Fig. 10 Comparisons between input and output motions

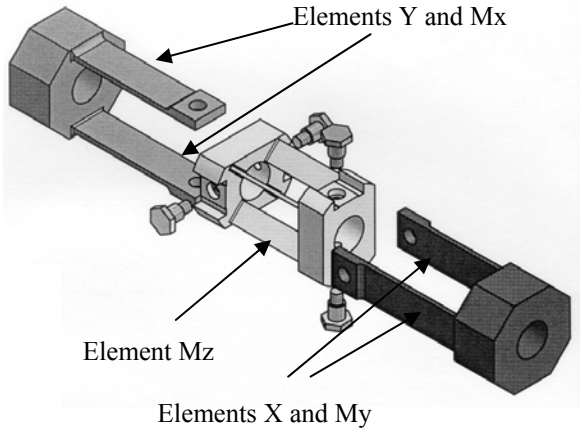

Fig. 11 Schematic of Bi-fold strain gauge balance before assembling

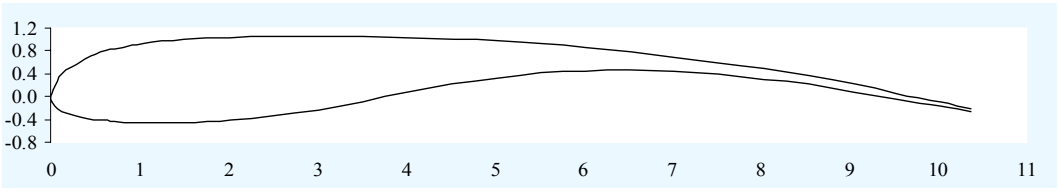

12a Section view of the test wing

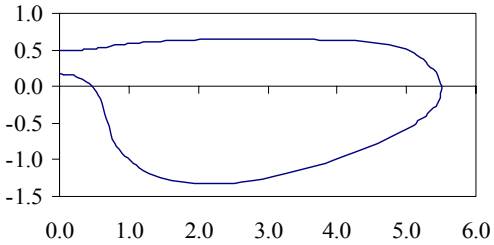

12b Plan view of the test wing

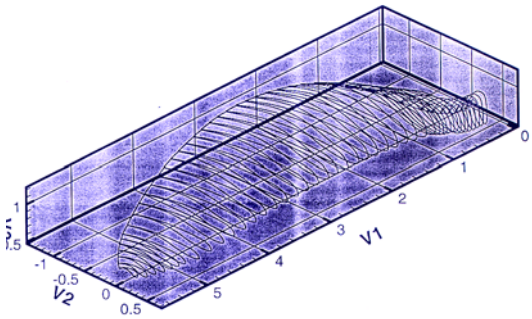

12c 3D view of the test wing

Fig. 12 Geometry of tested insect's wing

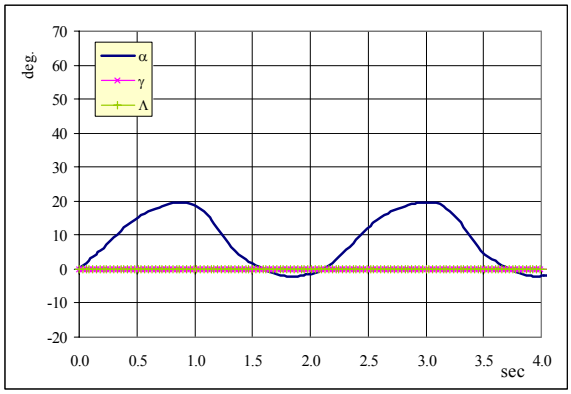

13a Motion profile

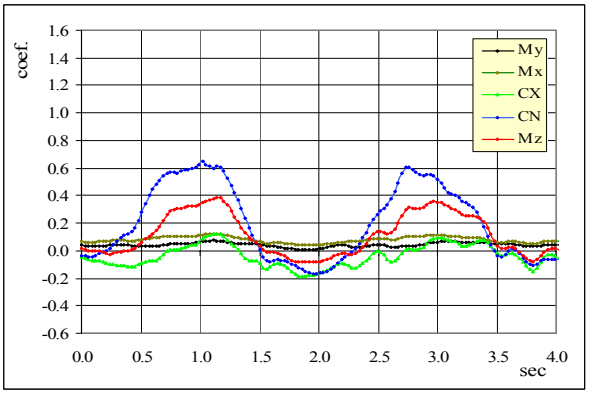

13b Measured aerodynamic coefficients

Fig. 13 One-degree-of-freedom motion and corresponding loads

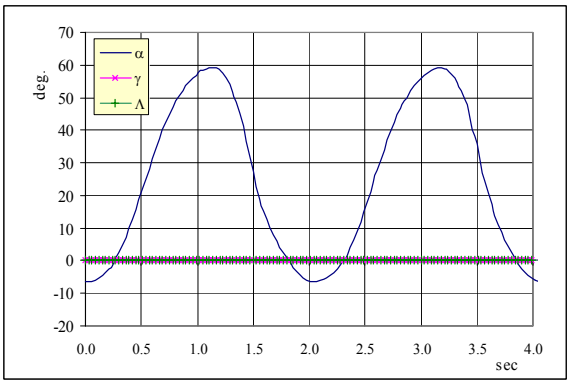

14a Motion profile

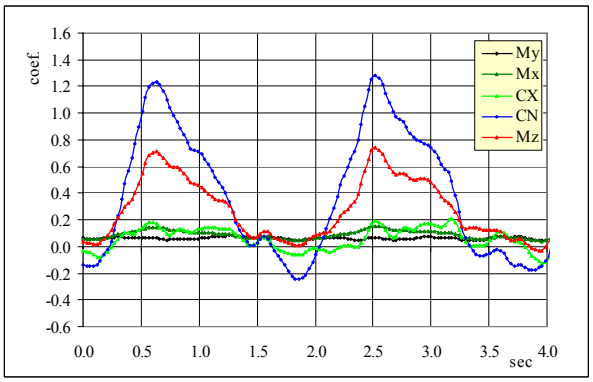

14b Measured aerodynamic coefficients

Fig. 14 One-degree-of-freedom motion and corresponding loads

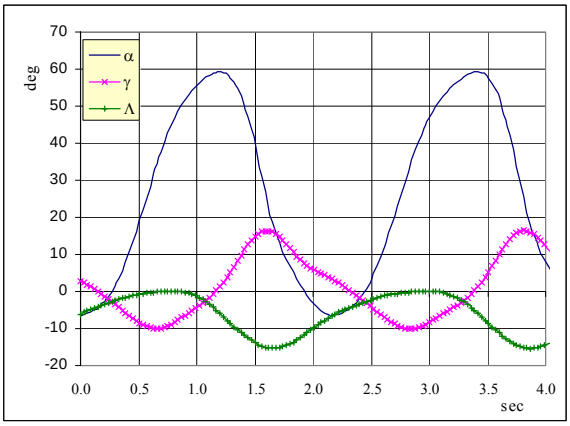

15a 3D motion history

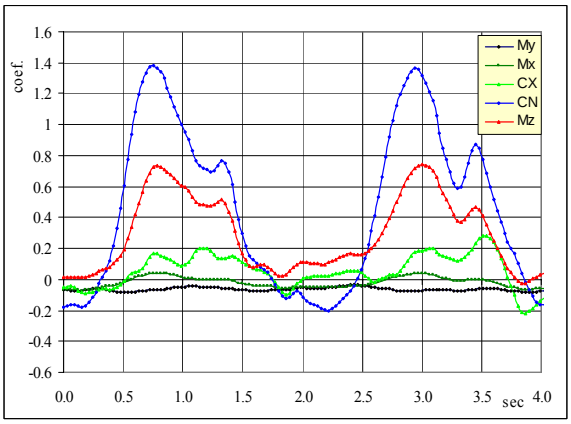

15b measured aerodynamic coefficients

Fig. 15 Three-degree-of-freedom motion and corresponding loads